Imaging interfaces defined by abruptly varying internal magnetic fields by means of scanned nanoscale spin wave modes

Chunhui Du, Inhee Lee, Rohan Adur, Yuri Obukhov, Christine Hamann, Bernd Buchner, Jeffrey McCord, Denis V. Pelekhov, and P. Chris Hammel

Phys. Rev. B **92**, 214413 — Published 9 December 2015

DOI: 10.1103/PhysRevB.92.214413

Imaging Interfaces Defined by Abruptly Varying Internal Magnetic Fields by Means of Scanned, Nanoscale Spin Wave Modes

Chunhui Du[1, †], Inhee Lee[1, 2, 3, †], Rohan Adur[1], Yuri Obukhov[4], Christine Hamann[5], Bernd Buchner[5], Jeffrey McCord[6], Denis V. Pelekhov[1, *], and P. Chris Hammel[1, *]

[1]*Department of Physics, The Ohio State University, Columbus, OH, 43210, USA*
[2]*Condensed Matter Physics and Materials Science Department, Brookhaven National Laboratory, Upton, New York 11973, USA*
[3]*Department of Physics, Laboratory for Atomic and Solid State Physics, Cornell University, Ithaca, NY 14853, USA*
[4]*HGST, San Jose, CA 95135, USA*
[5]*Institute for Metallic Materials, IFW Dresden, Postfach 270116, D-01171 Dresden, Germany*
[6]*Institute of Materials Science, Kiel University, Kaiserstrasse 2, 24143 Kiel, Germany*

[†]These authors made equal contributions to this work

*E-mails: pelekhov.1@osu.edu; hammel@physics.osu.edu

PACS numbers: 75.30.Ds, 07.79.−v, 75.75.+a, 75.78.-n

Abstract

Nanoscale devices fabricated out of magnetic heterostructures are central to the emerging field of spintronics, so understanding of magnetization dynamics at interfaces between dissimilar materials is essential. Here we report local imaging of magnetization dynamics at the interface formed by a sharp discontinuity in the magnetic properties of a ferromagnetic thin film using localized mode ferromagnetic resonance force microscopy (FMRFM). The behavior of the localized modes near the interface evolves with increasing magnitude of the FMRFM probe field due to its competition with the step-like internal demagnetizing field. We use micromagnetic modeling to visualize the evolution of localized mode as the magnetic probe is scanned across the interface. Our results demonstrate the ability to image sharp changes in internal magnetic properties in nanoscale devices and provide insights into the mechanisms underlying the generation and manipulation of localized modes near the interface, thus providing a new tool for microscopic studies of spin transport across magnetic interfaces and spin dynamics in their vicinity.

Magnetic multilayer nanostructures enabling the generation, transport, manipulation and detection of spin current are central to the emerging field of spintronics and the generation and control of spin current is an important topic of intense research [1, 2]. A common approach uses a ferromagnet to generate spin currents across the interface into the neighboring non-magnetic material by means of either a charge current driven through the statically magnetized ferromagnet [3, 4], or by spin pumping from the precessing magnetization [5-8]. Details of magnetization dynamics near interfaces are also important for spin torque oscillators [9-11] and magnonic crystals [12]. Thus, nanoscale mapping of both the local equilibrium magnetic properties of magnetic nanostructures, as well as spatially resolved characterization of dynamical properties in the presence of precessing magnetization in the vicinity of interfaces is essential.

Ferromagnetic Resonance Force Microscopy (FMRFM) exploits the spatially inhomogeneous magnetic field generated by a micromagnetic probe to spatially confine spin wave modes enabling microscopic imaging of the internal magnetic fields [13, 14] as well as local excitation of spin wave in order to probe local spin dynamics and transport in buried and exposed magnetic nanostructures [15-17].

Here we report nanoscale FMRFM imaging of magnetic properties and magnetization dynamics, using localized modes, in the vicinity of an interface with step-function internal field variation introduced through sample patterning. We find that the resonance conditions of the localized modes vary sensitively with proximity to the sharp shift of the internal field enabling nanoscale 2D imaging of the magnetic interface. Our micromagnetic modeling agrees well with the experimental data and enables detailed visualization of the evolution of the mode in the complex magnetic configurations. We find that tip-localized modes form under unexpected conditions in proximity to the interface. Moreover, our results demonstrate broad, in-situ

tunability of spin wave characteristics, including mode radius, position, and shape, by varying the total magnetic field experienced by the sample revealing additional approaches to localized mode generation. The ability to tailor the spin wave behavior in the vicinity of the interface can be valuable for spintronics applications where the spin injection efficiency has been shown to be dependent on the spin wave type and parameters [18-21]. This will also lead to improved measurement freedom in using FMRFM to study nanoscale magnetic systems.

To study the impact of abrupt magnetic field interfaces, a Ta (4 nm)/NiFe (Py, 20 nm)/IrMn (7 nm)/Ru (1-3 nm) multilayer was subjected to spatially patterned He ion bombardment with beam energy at 10 keV and an ion fluence of 1.2×10^{15} He cm^{-2} [22-24]. We find that ion irradiation alters the saturation magnetization of the Py film increasing it to $4\pi M_s = 10114$ G in irradiated (IR) regions, as compared to $4\pi M_s = 9719$ G in non-irradiated (NIR) region. This abrupt change of saturation magnetization produces a step-function variation of internal demagnetizing field of $\Delta 4\pi M_s \approx 400$ G when the film magnetization is saturated by an out-of- plane external magnetic field. The interaction antiferromagnetic with the IrMn layer produces an exchange bias field in Py layer, which is proved to be insignificant in our measurement geometry. Magnetic force microscopy (MFM) [Fig. 1(a)] of the interface demonstrates sharp contrast of the magnetic properties between the IR and NIR regions and a clear interface at $x = 0$.

Figure 1(b) shows the setup for our FMRFM experiment. The patterned Py thin film is glued on a microwave transmission line. A scanned probe is placed above the sample surface with a tunable probe-sample separation z. The micromagnetic probe is made by gluing a $SmCo_5$ magnetic particle of 1.48 μm in diameter at the end of a commercial Si cantilever [13]. The magnetic moment and coercivity of the particle are measured to be 1.2×10^{-9}emu and larger

than 20 kOe respectively by cantilever magnetometry [13, 25]. The probe magnetic moment is polarized in the direction opposite to the externally applied uniform magnetic field $\boldsymbol{H_0}$. The FMRFM signal is obtained at 10 K by measuring the cantilever oscillation frequency as a function of out-of-plane magnetic field H_0 in the presence of a fixed radio-frequency (rf) microwave magnetic field at ω_{rf} = 7.4719 GHz. The amplitude of the rf power is modulated at the mechanical resonant frequency of the cantilever (~10 kHz).

The ground state of the magnetization of a ferromagnetic film is determined by the total static magnetic field $\boldsymbol{H}_{\mathrm{stat}}(\boldsymbol{r})$ in the film [16]:

$$\boldsymbol{H_{stat}}(\boldsymbol{r}) = \boldsymbol{H_0} + \boldsymbol{H_p}(\boldsymbol{r}) + \boldsymbol{H_{demag}}(\boldsymbol{r}), \quad (1)$$

where $\boldsymbol{H}_0$ is the externally applied uniform magnetic field**,** $\boldsymbol{H}_{\mathrm{p}}(\boldsymbol{r})$ is the dipolar magnetic field of the probe and $\boldsymbol{H_{demag}}(\boldsymbol{r})$ is demagnetizing field of the sample. The exchange and magnetic anisotropy fields are not shown here for clarity. When sufficiently strong $\boldsymbol{H}_0$ is applied out of the film plane, it dominates other field contributions and the sample magnetization is also aligned out of the film plane. In this case, H_{demag} is mostly uniform, except for the region near the magnetic probe, and is equal to $\approx -4\pi M_s$. The spatial inhomogeneity of $\boldsymbol{H}_{\mathrm{stat}}(\boldsymbol{r})$, stemming from the spatial inhomogeneity of $\boldsymbol{H_p}(\boldsymbol{r})$ and $\boldsymbol{H_{demag}}(\boldsymbol{r})$ **,** results in spin wave localization [16]. As has been discussed in Ref.13 and 16, a localized FMR mode forms in the region of a sample where $H_{\mathrm{stat}}(\boldsymbol{r})$ is locally reduced by the antiparallel field from the probe forming what will hereafter be referred to as a well, i.e. a confined region in which the local internal static field is significantly weaker than elsewhere. This occurs beneath the magnetic probe magnetized antiparallel to the applied field such that its probe field $\boldsymbol{H_p}(\boldsymbol{r})$ partially cancels the externally applied uniform field $\boldsymbol{H_0}$. Consequently, the location and depth of the field well can be controlled by adjusting the lateral position of the probe x_{p} and the probe-sample separation z.

This enables the study of localized spin wave modes and high-resolution imaging of spin dynamics in various magnetic configurations.

In order to understand the behavior of localized FMR modes, it is important to understand the spatial profile of $\boldsymbol{H}_{\mathrm{stat}}(\boldsymbol{r})$ in the system under investigation. In our experiment the dynamics of the localized modes are determined by the relative magnitude of H_{p} and the magnitude of the variation of H_{demag} at the interface. We can identify 9 general patterns of $H_{\mathrm{stat}}(\boldsymbol{r})$, depending on the values of the z and the x_{p}, which are shown schematically in Fig. 1(c-k). Figures 1 (c,d,e) show the spatial variation of $H_{\mathrm{stat}}(\boldsymbol{r})$ at three different probe-sample separations when x_{p} = -10 μm far from the interface in the IR region, between two strips. In this region, the inhomogeneity of $\boldsymbol{H}_{\mathrm{stat}}(\boldsymbol{r})$ is dominated by $\boldsymbol{H}_{\mathbf{p}}(\boldsymbol{r})$, creating a field well with depth ΔH_{p} that localizes spin wave modes [13]. Figures 1 (i,j,k) show the variation of $H_{\mathrm{stat}}(\boldsymbol{r})$ in the NIR region at x_{p} = 10 μm. In this region the field well of $H_{\mathrm{stat}}(\boldsymbol{r})$ evolves similarly to the well shown in Figs. 1 (c,d,e) as the probe approaches the sample surface, except the overall $H_{\mathrm{stat}}(\boldsymbol{r})$ field is ~400 Oe higher than that in IR region due to the decreased magnetization, and hence reduced H_{demag} in the NIR region.

Figure 1(f,g,h) shows the evolution of $H_{\mathrm{stat}}(\boldsymbol{r})$ at x_{p} = 0, i.e., directly over the interface, as the probe-sample separation decreases, when both $\boldsymbol{H}_{\mathbf{p}}(\boldsymbol{r})$ and $\boldsymbol{H}_{\mathbf{demag}}(\boldsymbol{r})$ exhibit strong spatial variation. The magnetostatic mode behavior exhibits three qualitatively distinct behaviors as the probe approaches the sample surface; these three regimes are determined by the magnitude of ΔH_{p} relative to the discontinuity in $\Delta H_{\mathrm{demag}}$ field at the interface:

$$\begin{cases} z = 1650\ \mathrm{nm},\ \Delta H_{\mathrm{p}} < \Delta H_{\mathrm{demag}} & [\mathrm{Fig.\ 1\ (f),\ regime\ 1}] \\ z = 1125\ \mathrm{nm},\ \Delta H_{\mathrm{p}} \approx \Delta H_{\mathrm{demag}} & [\mathrm{Fig.\ 1\ (g),\ regime\ 2}] \\ z = 590\ \mathrm{nm},\ \Delta H_{\mathrm{p}} > \Delta H_{\mathrm{demag}} & [\mathrm{Fig.\ 1(h),\ regime\ 3}] \end{cases} . \qquad (2)$$

The competition between ΔH_{p} and $\Delta H_{\mathrm{demag}}$ controls the localized mode behavior and hence the ability to achieve high resolution imaging of the interfacial properties as we discuss below.

Figure 2 shows a series of FMRFM spectra measured for multiple probe-sample separations z with the probe located over the IR region of the sample far from the IR-NIR interface. In this case the spatial profile of $\boldsymbol{H}_{\mathrm{stat}}(\boldsymbol{r})$ is illustrated by Fig. 1 (c,d,e). All the spectra exhibit a similar peak at $H_0 \approx$12.7 kOe independent of z; this is the uniform mode resonance. As the probe approaches the sample surface, the depth of the field well increases resulting in mode localization. This effect manifests itself through the appearance of a negative-going peak, corresponding to the n=1 localized mode, whose resonant field H_{res} moves to higher applied field with decreasing z. This trend is expected due to the increasing depth of the localizing field well ΔH_{p} as the probe approaches the surface. The validity of this model is confirmed by the excellent agreement of the experimental data with the results of the micromagnetic modeling [16], obtained using the known experimental parameters, as shown in inset in Fig. 2. It can be seen that the uniform and the localized modes exhibit opposite signs of FMRFM signal reflecting the opposite signs of the gradient of the probe magnetic field at the respective locations of the modes thus confirming that these modes are spatially separated.

In order to image the interface with a step-like H_{demag}, we take FMRFM spectra as we scan the x_{p} across the interface. Figure 3 shows the resulting 2D field-position images for (a) z = 1650 nm, (b) z = 1125 nm, and (c) z = 590 nm, respectively. Figure 3 (a) corresponds to regime 1 (see eq. (2)) with ΔH_{p} = 170 Oe being much smaller than $\Delta H_{\mathrm{demag}}$. When the probe is in the IR region at x_{p} < -0.5 μm, the localized mode resonance field is almost constant $H_{\mathrm{res}} \approx$ 12.8 kOe. As the probe laterally approaches the interface, we observe localized mode resonance signals at both $H_{\mathrm{res}} \approx$ 12.4 kOe and $H_{\mathrm{res}} \approx$12.8 kOe. When x_{p} > 0.5 μm, only one localized mode with $H_{\mathrm{res}} \approx$

12.4 kOe is observed. At smaller probe-sample separation, z = 1125 nm, we are in regime 2 (see eq.(2)) where ΔH_{p} = 364 Oe is comparable to $\Delta H_{\mathrm{demag}}$ resulting in a 2D image shown in Fig. 3(b). When x_{p} < -0.5 μm, H_{res} is roughly constant at 12.9 kOe. At x_{p} = - 0.5 μm, two resonance signals appear with $H_{\mathrm{res}} \approx$ 12.9 kOe and 12.4 kOe, respectively. As x_{p} approaches the interface, the difference between those two resonance peaks decreases to around 200 Oe at x_{p} = 0.75 μm. For x_p > 0.75 μm, there is only one resonance at $H_{\mathrm{res}} \approx$ 12.5 kOe. Figure 3(c) shows the evolution of field-position image for regime 3 when ΔH_{p}= 997 Oe, much larger than $\Delta H_{\mathrm{demag}}$. In this case, there is always only one resonance detected. For x_{p} < 0, $H_{\mathrm{res}} \approx$ 13.4 kOe, then H_{res} gradually decreases to 13.0 kOe at x_{p} > 0.5 μm. The black squares in Fig. 3 from micromagnetic simulations agree well with our experimental data.

It can be seen in Fig. 3 that in all three regimes the localized modes behave very similarly when the probe is positioned far away from the interface whether in the IR or in NIR regions. In all the three cases, there is only one mode and the difference between the resonance fields of the modes in IR and NIR regions is ≈ 400 Oe, the magnitude of $\Delta H_{\mathrm{demag}}$ at the interface. However, the evolution of the localized mode resonant field, as the probe crosses the interface, demonstrates a very strong dependence on the z. This indicates that the formation of the localized mode is significantly different in the three regimes.

To understand the experimental results and visualize the evolution of localized mode behavior, we use micromagnetic simulations to calculate the effective field $H_{\mathrm{eff}} = {}^{\omega}/_{\gamma}$ [13, 16], and the spatial profile of localized modes at various x_{p} and z with selected results shown in Fig. 4. Our calculation of the spatial profile of $H_{\mathrm{stat}}(\boldsymbol{r})$ along the direction of the motion of the probe is

shown in Fig. 4. For clarity, all the calculations shown in Fig. 4 were performed using the same external field H_0 =13.2 kOe. The modelling results agree well with the experimental data.

Far from the interface, a single localized mode exists for all probe-sample separations, as seen in Fig. 4 (a,b,c), when the probe is located far away from the interface in either the IR or NIR regions and that it forms in the field well created underneath the micromagnetic probe. However the behavior at the interface is very sensitive to the strength of the probe field, that is, probe-sample separation. At small probe-sample separation, z = 590 nm, the probe magnetic field is strong enough that it dominates all other sources of field inhomogeneity. This produces a single localized mode in the interfacial region, as seen in Fig. 4c which is strongly distorted by the large, abrupt shift in the demagnetizing field at the interface producing a two-lobed spatial profile.

In contrast, in the weak and intermediate probe field regimes (regimes 1, z = 1650 nm and 2, z = 1125 nm respectively), modeling predicts the simultaneous existence of two localized modes on either side of the interface, even when the probe is directly over the interface (see the two middle columns in Fig. 4(a, b)). The calculated resonant fields of those modes agree well with the experimental measurements as shown in Fig. 3 (a,b) confirming the validity of the calculations. The observed modes are spatially separated with one mode located in the deep field well on the IR side of the interface while the other mode is situated on the NIR side of the interface where the demagnetizing field is distorted by the field of the probe. The existence of the mode on the IR side of the interface is expected since the mode is localized in a true field well. However on the NIR side of the interface, we find a striking and unexpected result: the appearance of a mode where no localizing well exists. This establishes new conditions under which a localized mode can be stabilized; this will open new directions of future studies.

Our FMRFM measurements have shown that the localized modes can be used for imaging internal magnetic fields at interfaces. Clearly, the strong probe magnetic field regime, shown in Fig. 3c, is preferred for high resolution imaging since the existence of a single localized mode in the vicinity of the interface simplifies interpretation of the data. The spatial resolution depends on the lateral position of the probe relative to the interface. When the probe located on the IR side, we demonstrate detection of an interface (assumed to be essentially infinitely sharp) with $\approx$100 nm resolution, while resolution on the NIR side is reduced to $\approx$500 nm due to the pinning of the localized mode at the interface.

We have demonstrated control over the size and location of spin wave modes in a Py film with particular attention to the important problem of modes near interfaces. Using FMRFM to perform magnetic resonance spectroscopy on these modes we image properties of the interface and reveal a strong sensitivity of the modes to local variation of magnetic properties. Our results provide a powerful method of understanding and controlling the characteristics of localized spin wave modes in strongly varying magnetic environments, a capability that could prove key to the study of static and dynamic spin properties in nanostructured systems.

Acknowledgements

This work was primarily supported by the US Department of Energy (DOE), Office of Science, Basic Energy Sciences, under Award No. DE-FG02–03ER46054 (FMRFM characterization and modeling). This work was also supported in part by the Center for Emergent Materials (CEM), an NSF-funded MRSEC under Award No. DMR-1420451 (development and implementation of materials growth, structural and magnetic characterization). This work was further supported in part by the German Science Foundation (DFG) under grant number MC9/7-2. This work was

supported in part by an allocation of computing time from the Ohio Supercomputer Center (micromagnetics calculations). We also acknowledge technical support and assistance provided by the NanoSystems Laboratory at the Ohio State University which is partially supported the CEM.

References:

1. J.C. Slonczewski, *J. Magn. Magn. Mater.* **159**, L1 (1996).

2. Y. Tserkovnyak, A. Brataas, G. E. W. Bauer, and B. I. Halperin, *Rev. Mod. Phys.* **77**, 1375 (2005).

3. Y. Fukuma, L. Wang, H. Idzuchi, S. Takahashi, S. Maekawa, and Y. Otani, *Nature Mater*. **10**, 527 (2011).

4. W. Han, R. K. Kawakami, M. Gmitra, and J. Fabian, *Nat. Nanotechnol.* **9**, 794 (2014).

5. Y. Kajiwara, K. Harii, S. Takahashi, J. Ohe, K. Uchida, M. Mizuguchi, H. Umezawa, H. Kawai, K. Ando, K. Takanashi, S. Maekawa, and E. Saitoh, *Nature* **464**, 262 (2010).

6. Y. Tserkovnyak, A. Brataas, and G. E. W. Bauer, *Phys. Rev. Lett.* **88**, 117601 (2002).

7. C. H. Du, H. L. Wang, Y. Pu, T. L. Meyer, P. M. Woodward, F. Y. Yang, and P. C. Hammel, *Phys. Rev. Lett.* **111**, 247202 (2013).

8. H.L. Wang, C.H. Du, Y. Pu, R. Adur, P.C. Hammel, and F.Y. Yang, *Phys. Rev. Lett.* **112**, 197201 (2014).

9. L. Liu, C.-F. Pai, D. C. Ralph, and R. A. Buhrman, *Phys. Rev. Lett.* **109**, 186602 (2012).

10. A. Hamadeh, O. A. Kelly, C. Hahn, H. Meley, R. Bernard, A. H. Molpeceres, V. V. Naletov, M. Viret, A. Anane, V. Cros *et al.*, *Phys. Rev. Lett.* **113**, 197203 (2014).
11. S. Bonetti, V. Tiberkevich, G. Consolo, G. Finocchio, P. Muduli, F. Mancoff, A. Slavin, and J. Åkerman, *Phys. Rev. Lett.* **105**, 217204 (2010).
12. A.A. Serga, A.V. Chumak, and B. Hillebrands, *J. Phys. D* **43**, 264002 (2010).

13. I. Lee, Y. Obukhov, G. Xiang, A. Hauser, F. Yang, P. Banerjee, D. V. Pelekhov, and P. C. Hammel, *Nature* **466**, 845 (2010).

14. Y. Obukhov, D. V. Pelekhov, J. Kim, P. Banerjee, I. Martin, E. Nazaretski, R. Movshovich, S. An, T. J. Gramila, S. Batra, and P. C. Hammel, *Phys. Rev. Lett*. **100**, 197601(2008).

15. R. Adur, C. H. Du, H. L. Wang, S. A. Manuilov, V. P. Bhallamudi, C. Zhang, D. V. Pelekhov, F. Y. Yang, and P. C. Hammel, *Phys. Rev. Lett.* **113**, 176601 (2014). .

16. C. H. Du, R. Adur, H. L. Wang, S. A. Manuilov, F. Y. Yang, D. V. Pelekhov, and P. C. Hammel, *Phys. Rev. B* **90**, 214428 (2014).

17. H.-J. Chia, F. Guo, L. M. Belova, and R. D. McMichael, *Phys. Rev. Lett.* **108**, 087206 (2012).

18. B. A. Kalinikos and A. N. Slavin, *J. Phys. C* **19**, 7013 (1986).

19. A. Kapelrud and A. Brataas, *Phys. Rev. Lett.* **111**, 097602 (2013).

20. H. T. Nembach, J. M. Shaw, C. T. Boone, and T. J. Silva, *Phys. Rev. Lett.* **110**, 117201 (2013).

21. S. A. Manuilov, C. H. Du, R. Adur, H. L. Wang, V. P. Bhallamudi, F. Y. Yang, and P. C. Hammel, *Appl. Phys. Lett.* **107**, 042405 (2015).

22. J. Fassbender and J. McCord, *Journal of Magnetism and Magnetic Materials* **320**, 579 (2008).

23. C. Hamann, R. Mattheis, I. Mönch, J. Fassbender, L. Schultz, and J. McCord, *New Journal of Physics* **16,** 023010 (2014).

24. J. W. Lau and J. M. Shaw, *J. Phys. D: Appl. Phys*. **44,** 303001(2011).

25. B. C. Stipe, H. J. Mamin, T. D. Stowe, T. W. Kenny, and D. Rugar, *Phys. Rev. Lett.* **86**, 2874 (2001).

Figure captions:

Figure 1. (a) MFM image of the sample, demonstrating the sharp contrast of magnetic properties between IR and NIR region. (b) Schematics of experimental configurations of FMRFM measurements. (c) to (k): Characteristic spatial profiled of internal static magnetic field $H_{\mathrm{stat}}(\boldsymbol{r})$ reflecting influence of the probe sample separation z and the probe lateral positions x_{p}.

Figure 2. FMRFM spectra of permalloy film in IR region measured at ω_{rf}= 7.4719 GHz and at several probe-sample separations *z*. In this measurement the probe was located far from IR-NIR interface. FMRFM spectra are offset for clarity. Inset: comparison of the experimental data and the micromagnetic modeling results for the resonant field of the first localized mode (n = 1), presented as a function of *z*, demonstrating an excellent agreement.

Figure 3. 2D FMRFM applied field – probe position images recorded for three probe-sample separations (a) z =1650 nm, (b) z =1125 nm, and (c) z =590 nm. Black squares represent the resonant fields of the localized modes obtained from micromagnetic simulations. The modelling results show excellent agreement with experimental data.

Figure 4. Numerically calculated spatial profiles of the modulus of the transverse magnetization of the localized modes and the corresponding cross section of the $H_{\mathrm{stat}}(\boldsymbol{r})$ calculated at four different lateral probe positions x_{p} for three probe-sample separations (a) z =1650 nm, (b) z =1125 nm, and (c) z =590 nm. All calculations were performed at constant field H_0= 13.2 kOe. Note the unique existence of a single mode even over the interface when the probe field is sufficiently strong (z=590 nm).

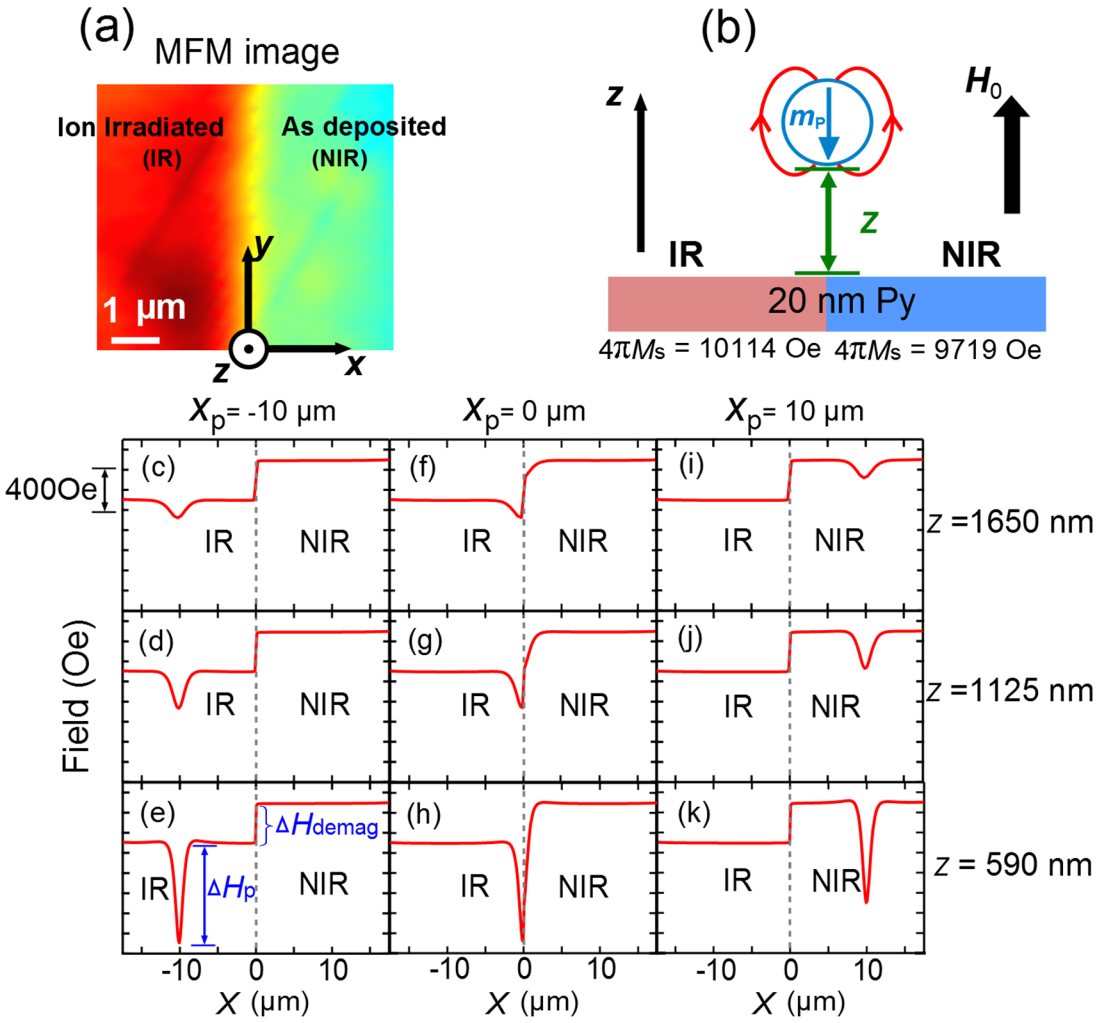
(a)
MFM image
Ion Irradiated
(IR)
As deposited
(NIR)
1 μm
y
z
x
(b)
z
m_P
H_0
z
IR
NIR
20 nm Py
$4\pi M_S$ = 10114 Oe
$4\pi M_S$ = 9719 Oe
X_p= -10 μm
X_p= 0 μm
X_p= 10 μm
400Oe
(c)
(f)
(i)
(d)
(g)
(j)
(e)
(h)
(k)
IR
NIR
ΔH_{demag}
ΔH_p
z =1650 nm
z =1125 nm
z = 590 nm
Field (Oe)
-10
0
10
X (μm)

Figure 1.

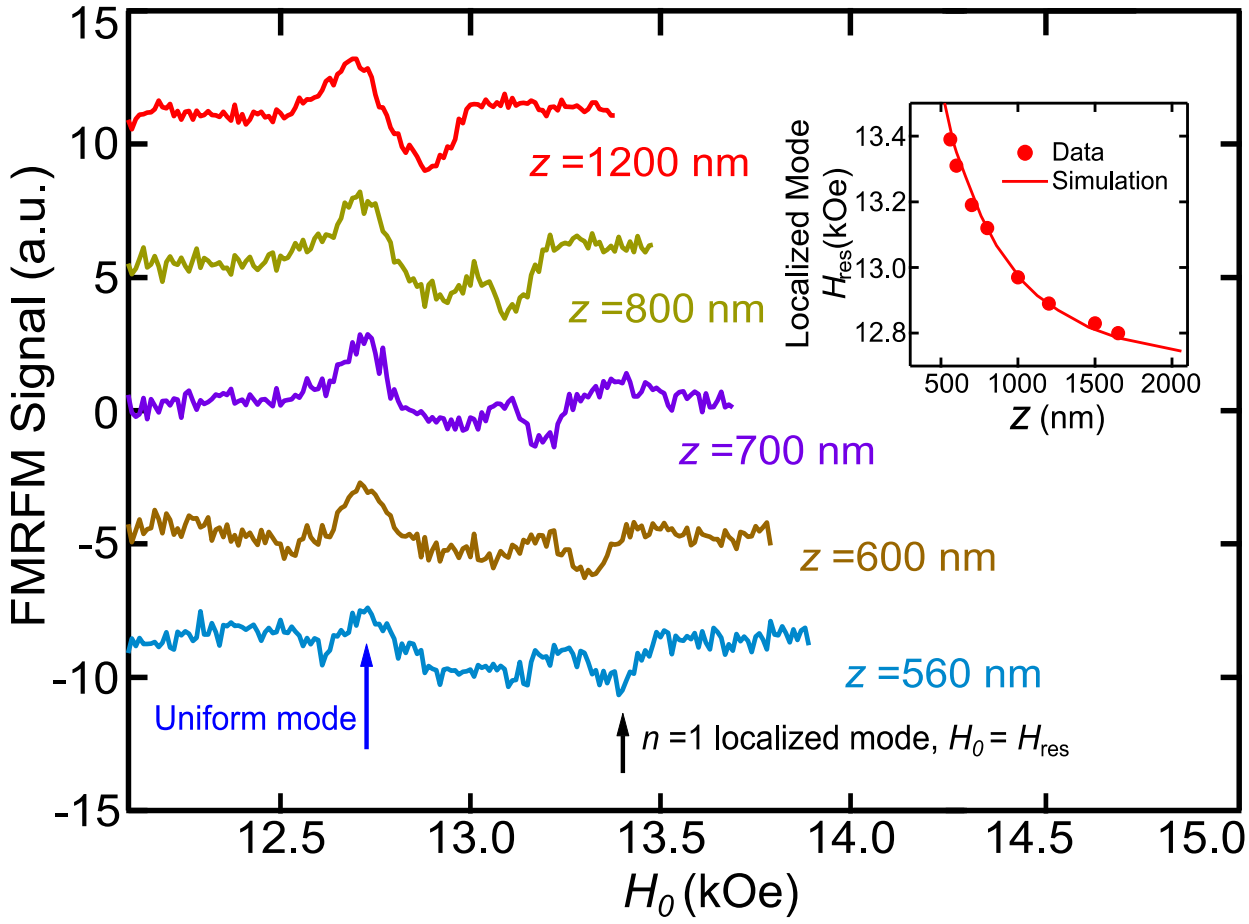
FMRFM Signal (a.u.)
15
10
5
0
-5
-10
-15
12.5
13.0
13.5
14.0
14.5
15.0
H_0 (kOe)
z =1200 nm
z =800 nm
z =700 nm
z =600 nm
z =560 nm
Uniform mode
n =1 localized mode, H_0 = H_{res}
Localized Mode H_{res}(kOe)
13.4
13.2
13.0
12.8
Data
Simulation
500
1000
1500
2000
z (nm)

Figure 2.

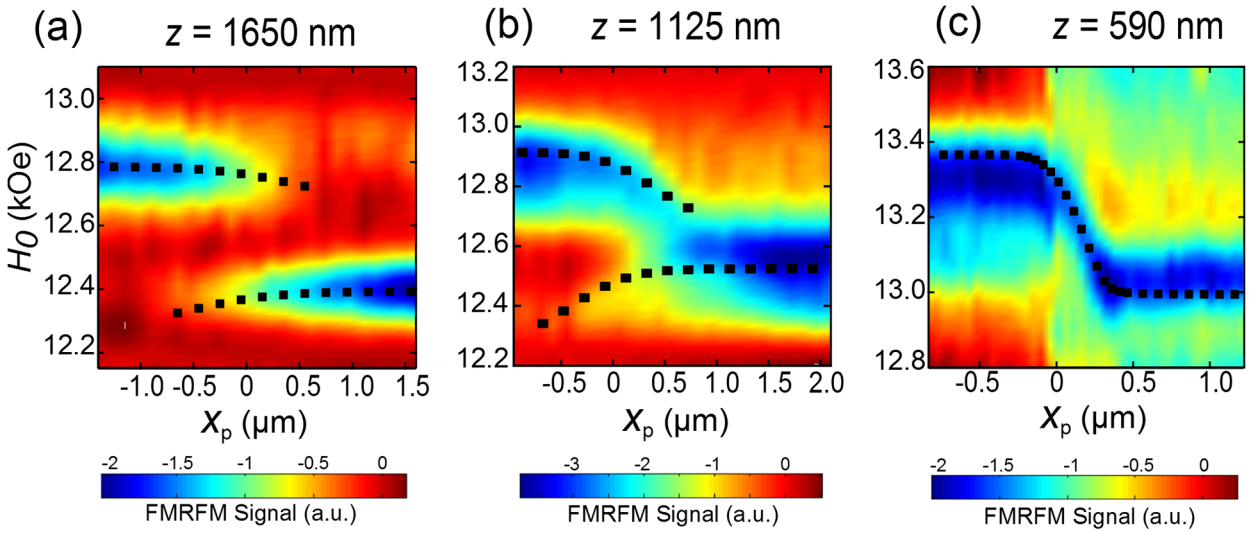

Figure 3.

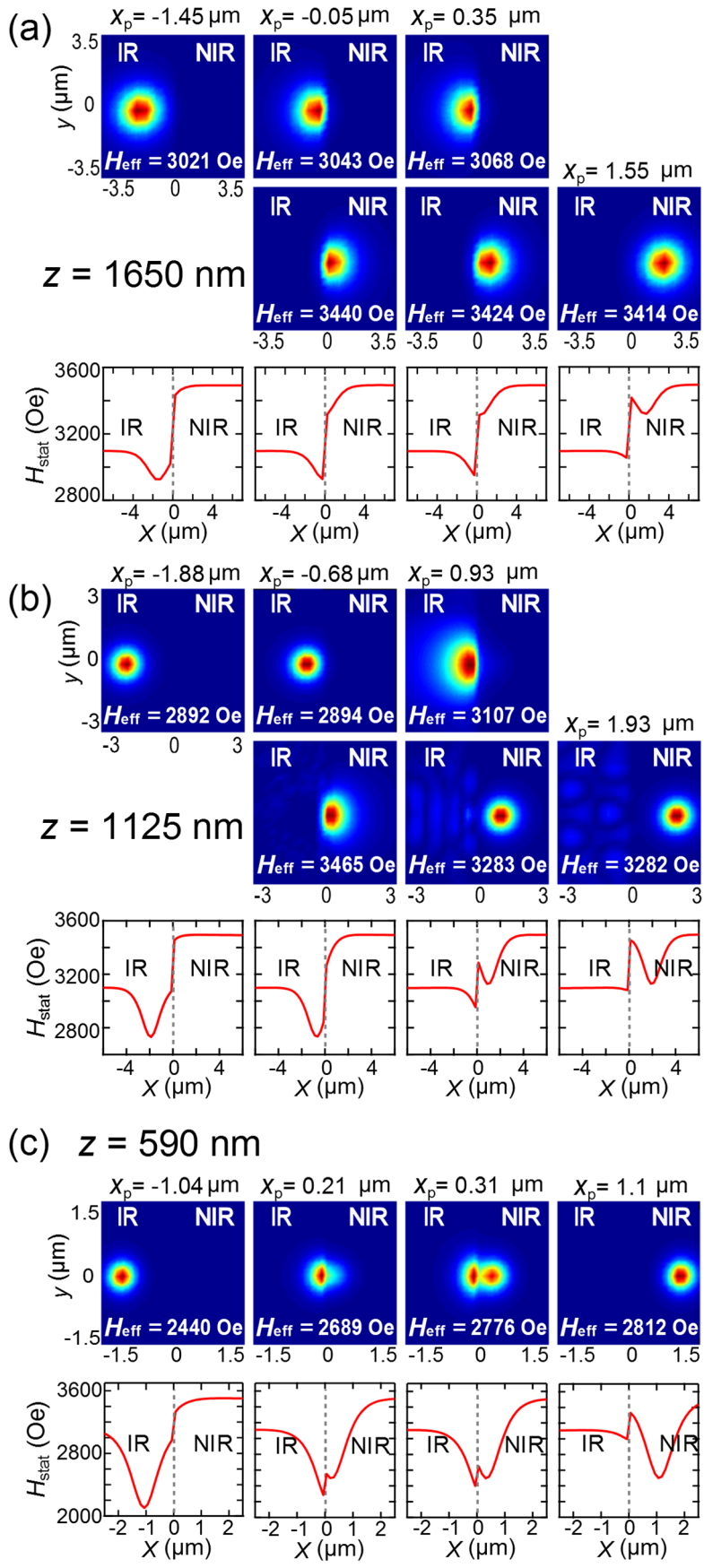
(a)
x_p= -1.45 μm
x_p= -0.05 μm
x_p= 0.35 μm
x_p= 1.55 μm
IR
NIR
H_{eff} = 3021 Oe
H_{eff} = 3043 Oe
H_{eff} = 3068 Oe
H_{eff} = 3440 Oe
H_{eff} = 3424 Oe
H_{eff} = 3414 Oe
y (μm)
z = 1650 nm
H_{stat} (Oe)
X (μm)
(b)
x_p= -1.88 μm
x_p= -0.68 μm
x_p= 0.93 μm
x_p= 1.93 μm
H_{eff} = 2892 Oe
H_{eff} = 2894 Oe
H_{eff} = 3107 Oe
H_{eff} = 3465 Oe
H_{eff} = 3283 Oe
H_{eff} = 3282 Oe
z = 1125 nm
(c) z = 590 nm
x_p= -1.04 μm
x_p= 0.21 μm
x_p= 0.31 μm
x_p= 1.1 μm
H_{eff} = 2440 Oe
H_{eff} = 2689 Oe
H_{eff} = 2776 Oe
H_{eff} = 2812 Oe

Figure 4.